Low Voltage and High-Speed Niobium Heterostructure Resistance Switching Memory Devices Integrating Ferro-Electric Enhanced Aluminum–Hafnium–Chromium–Aluminum Oxide

**LANCE LERUM, MOHAMMED FAHEM, OSAMA M. NAYFEH (Member, IEEE),
C. DAVE REES, KENNETH S. SIMONSEN, AND AYAX D. RAMIREZ**

SPAWAR Systems Center Pacific, San Diego, CA 92152, USA

CORRESPONDING AUTHOR: O. M. NAYFEH (e-mail: osama.nayfeh@navy.mil)

ABSTRACT Novel niobium heterostructure devices that integrate aluminum, hafnium, and chromium oxide are designed and constructed by sputtering and atomic layer deposition. The devices are examined for use in resistive switching (RS) memory cells. Specifically, $Nb–AlO_x–HfO_x–AlO_x–Nb$ is directly compared with $Nb–AlO_x–HfO_x–CrO_x–AlO_x–Nb$. Stable RS is observed in both cases and the conduction mechanisms are analyzed in detail. There are profound differences in the current (I–V) and capacitance (C–V) versus voltage characteristics with the insertion of CrO_x, including enhanced RS at reduced voltage and current and increased non-linearity in the C–V. The I–V characteristics are fitted to established conduction models and excellent agreement is obtained considering a Poole Frenkel emission and a Fowler Nordheim tunneling component that emerges strongly with increasing voltage. Direct quantum mechanical tunneling and ionic conduction currents are apparent, but weaker as expected with 6–8 nm film. The changes subsequent to RS, are captured with significant modification of the effective trap energy level, and density of the trap states' parameters and a small change in the electrode barrier height, supporting primary physical change in the properties of the bulk of the film stack and a minor change to the electrodes. Evidence of RS processes that involve both positively charged chromium and negatively charged oxygen ionic effects that effectively modify the current conduction are apparent. The plausible physical mechanisms that contribute to the RS are discussed in terms of changes to the bonding configuration and the active roles of ions and vacancies/defects in driving the formation and growth of conduction filaments. The impacts of ferro-electric like enhancements for devices that integrate CrO_x interfaced with HfO_x are considered and corroborated by measurements of the ferro-electric hysteresis loops that provide direct evidence of partial ferro-electric switching. Targeting low voltage and high speed operation, pulse measurements of $Nb–AlO_x–HfO_x–CrO_x–AlO_x–Nb$ devices, demonstrate capability to SET/RESET with <50 ns pulses and potential for excellent endurance and nonvolatile retention times. With liquid nitrogen cooling, RS properties are retained with a consistent reduction of the thermally dependent current conduction components as compared to the tunneling.

INDEX TERMS Resistive switching, memory, niobium, heterostructures, transport conduction, Poole Frenkel, tunneling, ferro-electrics, cryogenic, atomic layer deposition, sputtering, hafnium oxide, aluminum oxide, chromium oxide.

I. INTRODUCTION

There is a need for the design and implementation of memory devices compatible with quantum computing and superconducting digital computing technologies as well as low voltage logic transistors based on tunneling processes. Niobium (Nb) is typically used to construct Josephson

junctions used in qubits [1], [2], rapid single flux quantum (RSFQ) logic [3], [4] and more recently cryogenic compatible digital memory options for superconducting computing [5]–[9] and emerging quantum memory concepts that harness the quantum mechanical regime of operation [10]. While most investigations examine Nb devices, e.g., $Nb-AlO_x-Nb$ in the superconducting regime of operation, this work examines the room temperature conduction and RS properties of Nb heterostructures that integrate aluminum, hafnium and chromium oxide thin films formed by atomic layer deposition (ALD) and sputtering. This investigation aims to provide insights into the device operation and heterostructure properties relevant to the design of future memory and qubit devices. Interestingly, to the best of our knowledge, there are no or very limited experimental confirmations on the use of Nb metal as the electrodes in room temperature resistive switching memory (ReRAM)/memristor devices [11]–[25]. As there is no guarantee that with integration of a specific electrode or using a unique fabrication process that RS functionality would be retained, it warrants experimental confirmation. There is also a need to further reduce the switching voltage and speed of ReRAM to ensure compatibility with logic device technologies and improve energy efficiency [24], [25]. The devices examined are carefully designed to result in reduced voltage nonvolatile RS by harnessing ferro-electric enhancements with CrO_x interfaced with the HfO_x. In addition, these devices are designed for compatibility with superconductor electronics process integration and excellent memory performance, by using Nb electrodes and AlO_x barriers versus the other metal electrodes and barriers typically used in ReRAM. While there are promising Nb devices currently under evaluation for use as cryogenic memories for superconducting computing [5]–[7], these devices typically require magnetic multi-layer film stacks that can be prone to non-uniformity, or are not entirely electric field-controllable with voltage. A low voltage, and electronically switchable Nb memory technology would therefore be advantageous as an alternative option for compatibility with superconductor electronics (SCE) processes. It is therefore necessary to investigate alternative heterostructure designs and experimental validations.

The measured I-V characteristics for the heterostructure devices examined are modeled excellently when considering Poole Frenkel (PF) type emission and Fowler Nordheim (FN) tunneling as the primary conduction mechanisms as well as lower magnitude direct quantum mechanical tunneling (DT) and ionic conduction current component (IT). This analysis supports the plausibility that several physical mechanisms contribute to the total RS behaviors under the measurement conditions examined, and can account for the major differences with integration of CrO_x. These likely appear as the result of changes to the bonding configurations in the bulk of the film stack and interfaces that modify the current conduction. There is a drive towards chromium and oxygen ion migration and the formation of vacancies and conduction

filaments where under high current conditions there is a competition of these effects. Given the profound differences with CrO_x inserted in the heterostructure, this analysis supports the notion that current modulations due to ferro-electric like effects impact the RS and consistent with observed partial switching in the measured ferro-electric polarization loops. This is especially true for the case of $Nb-AlO_x-HfO_x-CrO_x-AlO_x-Nb$, where a strong RS is observed at reduced voltage and current. The plausible physical effects responsible for the conduction are discussed in accordance to model fittings, energy-band diagrams and a physical model. These results encourage further validation into the physical phenomenon responsible for the RS by atomistic simulations and in-situ spectroscopy. To evaluate potential performance for nonvolatile memory cells, low voltage and high speed pulsed measurements of $Nb-AlO_x-HfO_x-CrO_x-AlO_x-Nb$ demonstrate excellent retention times and endurance with sub-50 ns SET/RESET pulses.

II. DESIGN CONSIDERATIONS

The devices examined include heterostructure devices formed by sputtering and ALD that integrate Nb metal, aluminum, hafnium and chromium oxides. These specifically include $Nb-AlO_x-HfO_x-AlO_x-Nb$ and comparison with the case of an inserted CrO_x film, i.e., $Nb-AlO_x-HfO_x-CrO_x-AlO_x-Nb$. The heterostructures are selected towards a well-designed voltage controllable memory device that can be constructed with Nb fabrication process technology as described in [3], [4]. HfO_x is selected due to its well-established RS response at 1-2 V as examined recently by several groups with several electrode material options [17]. Despite the successes with HfO_x, there is a drive to further reduce voltage for energy efficiency and to maintain compatibility with sub-1 V operation of silicon based logic [26], [27] and towards the operating conditions of SCE [8], [9]. The AlO_x barriers between the Nb electrodes and HfO_x are inserted due to the well-known compatibility of Al compounds with Nb [3], [4] and their potential to enhance device performances [28], due to the presence of conduction and valence band off-sets with respect to relatively smaller energy gap HfO_x [29]. The 2-2-2 nm ALD films are selected out of consideration for proper memory device engineering [30]. CrO_x is selected and interfaced with HfO_x due to the potential for ferro and magneto-electric enhancements in speed and voltage in a film that can be readily deposited by sputtering or ALD [31], [32] and that may enable enhanced RS processes as compared to conventional filament driven process. Very recent studies have provided corroborating evidence of a ferro-electric like modulation of RS, specifically with the integration of Hf compounds [33], [34]; these effects are a topic of intense investigation in the community.
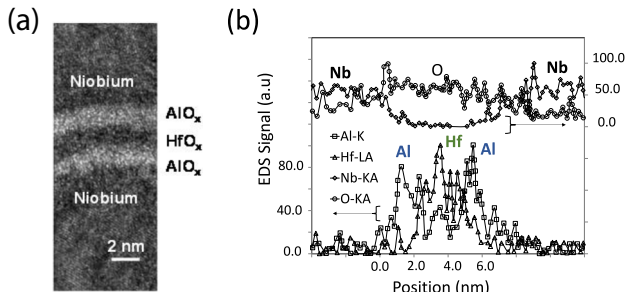
III. EXPERIMENT AND RESULTS
A. FABRICATION
The device fabrication process combines sputtering and ALD, and is performed in a class 100 clean-room. Substrates
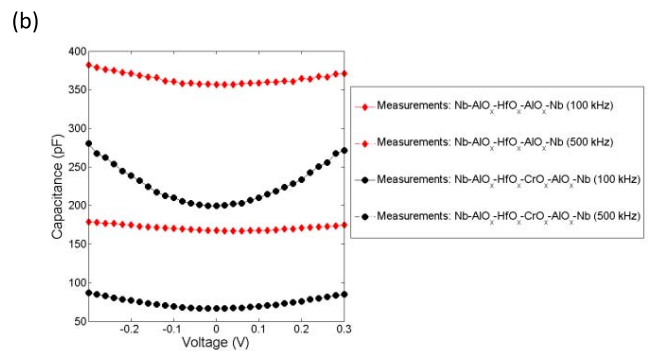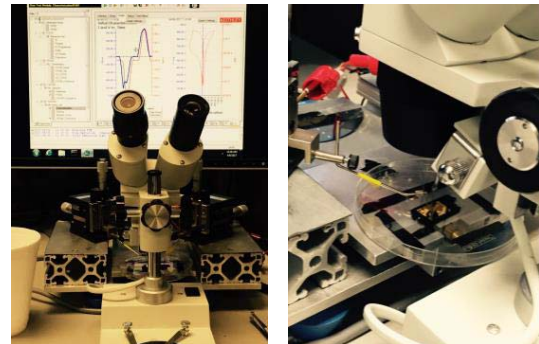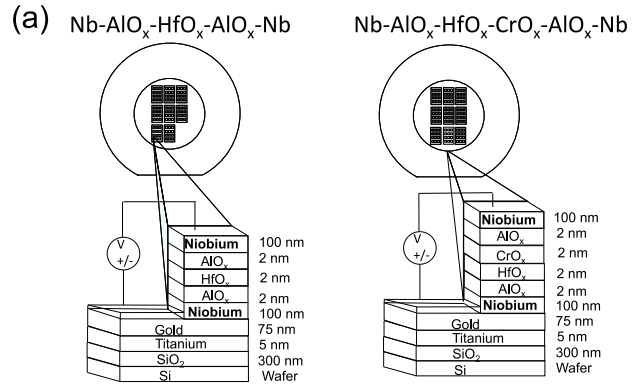
are 4" silicon wafers from University Wafer with 300 nm of thermal SiO_2. Five and 75 nms of titanium and gold (for bottom electrode contact) are RF and DC sputtered in the presence of argon with a Denton Discovery 18 sputtering tool followed by DC sputtering at 200 watts in argon of 100 nm Nb bottom electrodes under similar conditions to those found in reports in [35]. A 2-2-2 nm (20-20-20 cycle) AlO_x-HfO_x-AlO_x heterostructure is subsequently formed by ALD at 200 °C with a Beneq TF 200 in thermal mode using H_2O, trimethylaluminium (TMA) and tetrakis(dimethylamino)hafnium (TDMAH) precursors in accordance with processes described in [36] and elsewhere. To produce Nb-AlO_x-HfO_x-CrO_x-AlO_x-Nb, select wafers are removed from the ALD chamber after HfO_x deposition and 2 nms of CrO_x are deposited by the reactive RF sputtering of chromium at 100 watts in a 95% Ar/5% O_2 mixture. Following sputtering of CrO_x, a 2 nm AlO_x cap is subsequently deposited by ALD. Care is taken to minimize within wafer exposure time to 15-20 minutes, to ambient upon insertion and re-insertion between the sputtering and ALD chambers. Top Nb electrode metal of 100 nm is then DC sputtered and devices are patterned and defined with conventional photolithography with an MA6 mask aligner and subsequent SF_6 dry-etching in an Oxford Plasmalab80 etcher producing devices with dimensions.

FIGURE 1. (a) HR-XTEM image of a typical Nb-AlO_x-HfO_x-AlO_x-Nb heterostructure produced by the sputtering and ALD process (b) EDS spectra across the film stack and the extracted Nb, O, Al, and Hf elemental contributions. The ALD AlO_x-HfO_x-AlO_x films are 2-2-2- nm respectively.

High resolution cross sectional transmission electron microscopy (HR-XTEM) and associated energy dispersive spectroscopy (EDS) for a typical Nb-AlO_x-HfO_x-AlO_x-Nb film stack are obtained and presented in Figure 1a and Figure 1b. The XTEM and EDS measurements confirm the Nb, Al, Hf and O elemental compositions and respective film thicknesses. It is apparent that after completion of the device fabrication process, there remains a clear separation between the AlO_x, HfO_x and AlO_x films that determine the heterostructure. While not readily resolvable by EDS, it is expected that some degree of chemical modification may occur at the interfaces present in the Nb-AlO_x-HfO_x-AlO_x-Nb film stack. While XTEM is not obtained for the case of Nb-AlO_x-HfO_x-CrO_x-AlO_x-Nb, it is inferred that the ALD films are of a similar quality. However, as a consequence

of the sputtering process of the CrO_x and the unavoidable exposures to ambient when moving wafers between the sputtering and ALD tools, it is reasonable to expect that more significant modification may occur.

FIGURE 2. (a) Schematics and measurement configuration for both Nb-AlO_x-HfO_x-AlO_x-Nb and Nb-AlO_x-HfO_x-CrO_x-AlO_x-Nb heterostructure devices (b) C-V measurements at 100 and 500 kHz spanning -0.3 to 0.3 V taken on a device with dimensions of 250 μm x 250 μm.

B. ELECTRICAL MEASUREMENTS (DC)

The current and capacitance versus voltage (I-V and C-V) characteristics are measured in a room temperature probe station with a Keithley 4200 semiconductor characterization system as described in the schematics in Figure 2a with voltage applied between top and bottom electrodes. The C-Vs of the heterostructure devices spanning -0.3 to 0.3 V and at 100

and 500 kHz are plotted in Figure 2b. For Nb-AlO$_x$-HfO$_x$-AlO$_x$-Nb, very low levels of capacitance modulation with voltage is observed. For the case of Nb-AlO$_x$-HfO$_x$-CrO$_x$-AlO$_x$-Nb, a 15% reduction in total capacitance is observed that is consistent with 2 nm of CrO$_x$ inserted in the film stack and a commensurate decrease in the effective permittivity from 10.0 to 8.8. The increased dispersion between measurements taken at 100 and 500 kHz and the non-linearity in the C-Vs is explainable by an increased dielectric relaxation due to increased metallic (Cr) content as described in [37], and the possibility of ferro-electric-like effects as a direct consequence of the inserted CrO$_x$ [31], [32] film in the stack or introduced by an effective Cr doping at the CrO$_x$-HfO$_x$ interface [33], [34]. This possibility will be discussed in more detail in the next section.

I-V measurements of a representative device are collected at room temperature sweeping the voltage forward and reverse from -1V to 1V and back to -1V with the compliance current set by the instrument at 1 mA and 10 mA. It is well known that specific RS physical mechanisms are strongly impacted by the voltage/electric-field and the current flow [11]–[25], so this analysis is limited to the technologically relevant regime spanning +/- 1V [25]. Focus is made on 250 μm x 250 μm devices that are amenable to characterization with the equipment with 85% of the devices on wafer are functional.

Figure 3 presents typical (DC) I-V measurements for the Nb-AlO$_x$-HfO$_x$-AlO$_x$-Nb heterostructure device with current compliance set at a) 1 mA and b) 10 mA. With 1 mA, <1% of current switching is observable and current compliance is quickly approached with operating voltage of 0.1 V. With 10 mA current compliance, Nb-AlO$_x$-HfO$_x$-AlO$_x$-Nb devices have a pronounced RS observed as sharp drops and jumps in current at +0.98 and -0.78 V. These jumps and drops are what would be considered as a SET and RESET in a memory device. The asymmetry in SET/RESET voltage is likely a consequence of the process sequence and exposure to ambient and plasma especially at the top AlO$_x$-Nb interface and possible modification to the effective bottom electrode metal work-function due to the presence of the gold in contact to the Nb [38]. Note that the observed RS behavior in these measurements does not require a pre-sweep (higher voltage/current) forming, as is often required with many other film and electrode combinations reported in [24]. Under the measurement conditions reported here, there is a net counter clockwise hysteresis with nearly two orders of magnitude current switching and an effective modulation of the high/low resistance of 75 at 0.2 V. The RS behavior in Nb-AlO$_x$-HfO$_x$-AlO$_x$-Nb is similar to that observed by other groups for devices that integrate ALD HfO$_x$ films and several metal electrode options [24], [25]. However, according to the current physical understanding of RS processes, there is no guarantee that with integration of a specific electrode or combination of electrodes, RS behavior would be retained, as it can be strongly impacted by the physical properties of the electrodes [24], especially if they are prone to,

for example, oxidation/reduction from migrating ions. To the best of our knowledge these experimental results in this work are the first validation of a strong RS behavior at room temperature in devices that integrate Nb metal electrodes and motivates continued research and development to optimize it for memory applications.

(a)

(b)
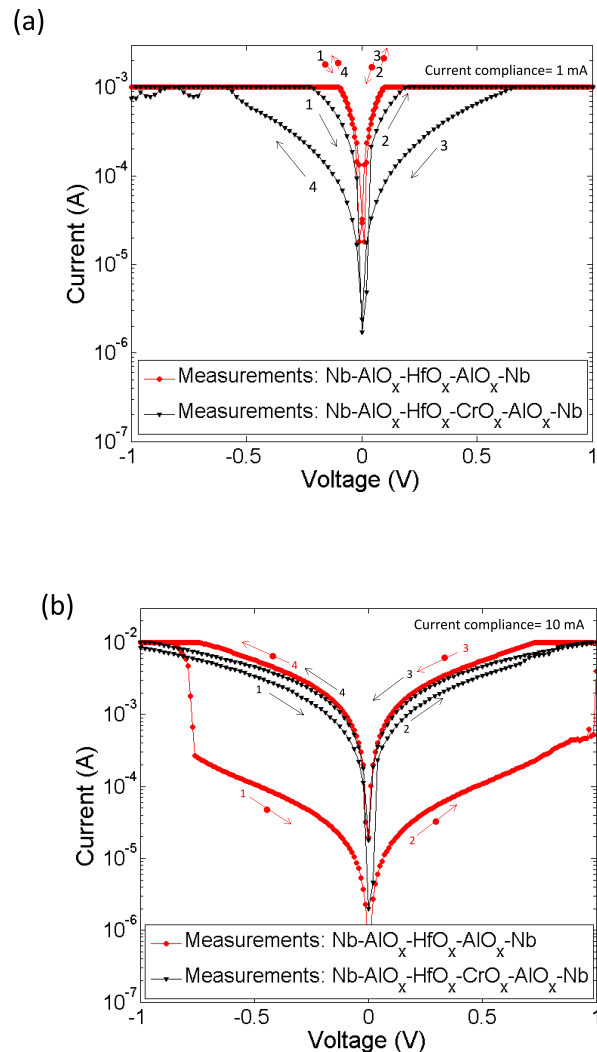
FIGURE 3. Experimental (DC) room temperature I-V characteristics under forward and reverse sweeping spanning -1V to 1V and back to -1V for Nb-AlO$_x$-HfO$_x$-AlO$_x$-Nb and Nb-AlO$_x$-HfO$_x$-CrO$_x$-AlO$_x$-Nb. The current compliance is set to a) 1 mA and (b) 10 mA. Device dimensions are 250 μm x 250 μm.

The I-V measurements, i.e., with current compliance set to 1 mA and 10 mA are taken with the identical methods for the case of the heterostructures with an embedded CrO$_x$ film, (i.e., Nb-AlO$_x$-HfO$_x$-CrO$_x$-AlO$_x$-Nb), and are plotted for direct comparison with Nb-AlO$_x$-HfO$_x$-AlO$_x$-Nb in Figure 3a and Figure 3b. As presented in Figure 3a, (and under 1 mA compliance current conditions), a profoundly different behavior is observed with insertion of CrO$_x$. This includes observation of a strong RS and near order of magnitude current switching resulting in consistent clockwise

hysteresis. The RS in this device is not sharp, but gradual across the 0.5 V range. By increasing the current compliance to 10 mA (Figure 3b) and approaching 1 V, the Nb-AlO$_x$-HfO$_x$-CrO$_x$-AlO$_x$-Nb heterostructure has a weak RS with a net counter-clockwise hysteresis and less than a 1.4x switching in current and this behavior (under higher current) suggests a balance between the contributions of the RS effects stemming from both the CrO$_x$-HfO$_x$ and AlO$_x$-HfO$_x$ in this device. The strong RS effects observed at <0.5 V with insertion of CrO$_x$, suggests the plausibility of alternative mechanisms than the conventional filamentary RS processes typically observed for HfO$_x$, and requiring 1-2 V. The plausible physical interpretations for the RS are discussed in the next section and are supported by fittings of the I-V characteristics to several current conduction models, a band diagram and a physical description that considers chromium and oxygen ionic effects, vacancy and conduction filament formation and the interesting possibility of a ferro-electric like effect at the CrO$_x$-HfO$_x$ interfaces.

C. HIGH-SPEED PULSED MEASUREMENTS

High speed pulsed measurements with repeated cycling up to 10^5 cycles and down to 20 ns pulse width/rise/fall times are obtained for Nb-AlO$_x$-HfO$_x$-CrO$_x$-AlO$_x$-Nb. Measurement data is collected with the Keithley 4200 semiconductor characterization system with a 4225-PMU ultra-fast pulse measure unit. Figure 4a presents data taken with 20 ns pulse width/rise/fall times spanning -0.25 V to 0.25 V with the current compliance set to 1 mA. The timing diagram for the pulses is shown in the inset. Consistent RS with the DC case is clearly observed under these conditions supporting a high speed and low voltage RS process in these devices. Current compliance is not reached under these conditions. The RS behavior is stable with cycling up to 10^5 cycles with fluctuations in the minimum currents likely from thermal or volatile trapping/de-trapping events or of other non-idealities including displacements especially with the presence of ferro-electric behavior. Next, the voltage span is increased to -1 to 1 V and the measurements are repeated with the identical timing sequence and presented in Figure 4b. Stable RS is also observed up to 10^5 cycles and current compliance of 1 mA is nearly reached. Similar behavior and reaching current compliance is obtained with 50 ns pulse width/rise/fall times as shown in Figure 4c. The low voltage, high-speed and stable RS is consistent with a nondestructive processes that result in the RS processes in these devices. The operation at micron scale required for RS in these devices is also useful for understanding potential operating conditions of scaled devices, however at the nanoscale it is expected that parasitic elements will likely have a greater contribution and may set the required total RS switching current.

D. CRYOGENIC LIQUID NITROGEN (LN$_2$) CHARACTERIZATION

Nb-AlO$_x$-HfO$_x$-CrO$_x$-AlO$_x$-Nb devices are cooled by immersion in liquid nitrogen as shown in the experiment
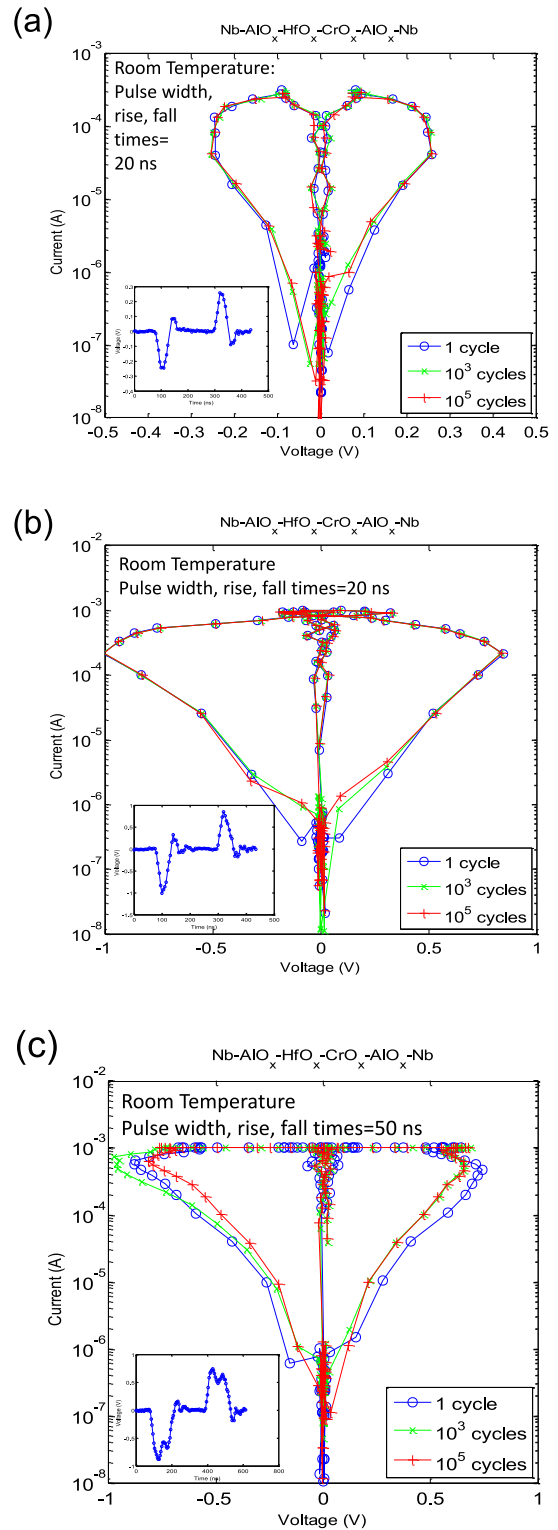
FIGURE 4. Pulsed I-V measurements of Nb-AlO$_x$-HfO$_x$-CrO$_x$-AlO$_x$-Nb with (a) 20 ns pulse width/rise/fall times spanning -0.25 V to 0.25 V (b) 20 ns pulse width/rise/fall times spanning −1 V to 1 V (c) 50 ns pulse width/rise/fall times spanning −1 V to 1 V.

setup in Figure 2b and measurements are taken for two cooldowns. I-V measurements are quickly collected under cooled conditions and upon return back to room temperature and
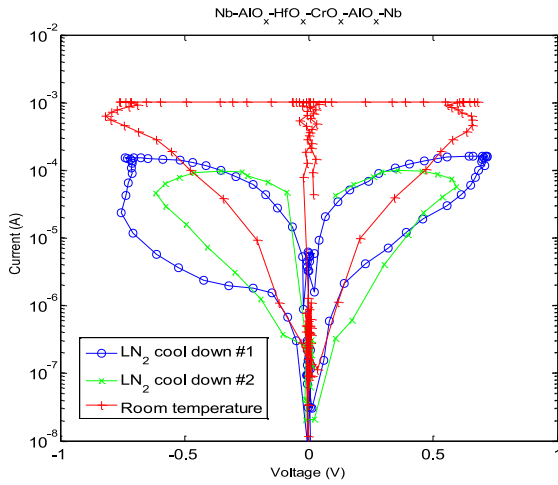
FIGURE 5. Pulsed I-V measurements of Nb-AlO$_x$-HfO$_x$-CrO$_x$-AlO$_x$-Nb with liquid nitrogen cooling with 50 ns pulse width/rise/fall times. Shown are data for two cool-downs and upon warming back to room temperature.

FIGURE 6. Ferro-electric polarization hysteresis loops taken at room and liquid nitrogen temperatures for Nb-AlO$_x$-HfO$_x$-CrO$_x$-AlO$_x$-Nb and compared with Nb-AlO$_x$-HfO$_x$-AlO$_x$-Nb. For the case of CrO$_x$ devices there is ferro-electric like behavior with a remnant polarization at near 0 V.

are presented in Figure 5. While RS is retained demonstrating potential for cryogenic compatibility in these devices, there is clear reduction in the current levels and in the voltage of the *I-V* characteristics consistent with reduction in the thermal processes that impact the current conduction with cooling. This notion will be analyzed and further corroborated in accordance with the thermal and tunneling conduction current models in the next section.

E. FERRO-ELECTRIC LOOPS
Ferro-electric polarization loops are measured with a Keithley 4220 + PMMU and are presented in Figure 6 and comparison between Nb-AlO$_x$-HfO$_x$-AlO$_x$-Nb and Nb-AlO$_x$-HfO$_x$-CrO$_x$-AlO$_x$-Nb to validate possibility of ferro-electric like effects. For the case of Nb-AlO$_x$-HfO$_x$-AlO$_x$-Nb capacitive type behavior is observed without clear evidence of any remnant polarization. In contrast, for Nb-AlO$_x$-HfO$_x$-CrO$_x$-AlO$_x$-Nb, an additional ferro-electric like behavior is observed in the polarization loops. While the loops are not as ideal as, e.g., bulk PZT, there are clear signs of remnant polarization and curvature even in these thin 8 nm films, strongly suggesting ferro-electric like behavior. Under liquid nitrogen conditions the polarization loops become more ideal in shape and the remnant polarization remains relatively constant.

F. MEMORY RETENTION AND ENDURANCE
To evaluate nonvolatile memory performance potential of these devices, standard endurance and retention time data are obtained up to 10^5 cycles and 10^5 seconds. Read of the current state is taken at 0.08 V to minimize impacts of measurement that can accelerate loss of retention. The measurements are presented in Figure 7. Endurance is excellent with very stable high SET/RESET current states. Some fluctuation in the lower current state as observed is apparent as observed in the I-V characteristics. Retention times for
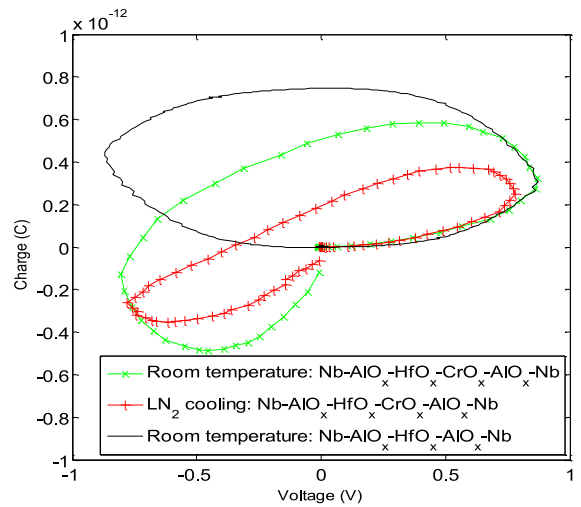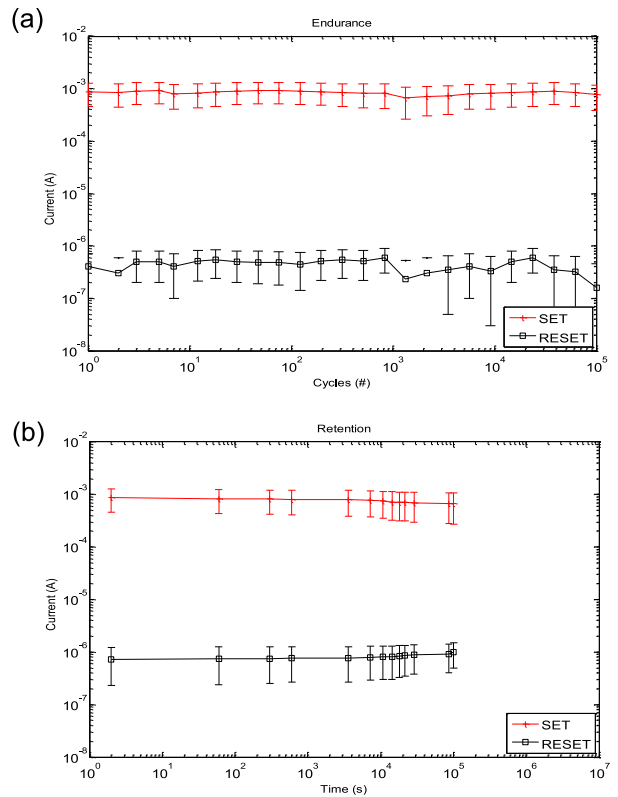
FIGURE 7. Endurance and retention times for Nb-AlO$_x$-HfO$_x$-CrO$_x$-AlO$_x$-Nb with SET/RESET voltages of +/- 1V using pulse width/rise/fall times of 50 ns. Read of the memory state is measured at 0.08 V. Error bars are obtained after repeating this measurement 4 times.

both high current and low current states have 10 and 15% decay after 10^5 seconds (28 hours) at room temperature. Also shown in the plot are the extrapolation which shows potential for >10 years storage times.

IV. ANALYSIS AND DISCUSSION

A. CONDUCTION MODELING

Insight into the room temperature conduction mechanisms and RS processes are obtained by fitting the measured I-V characteristics with established conduction models and constructing the energy band diagrams. The necessary changes required to the model parameters in order to capture the RS processes, (i.e., the difference in the I-Vs comparing forward and reverse sweep directions) are evaluated and provide insight on the physical mechanisms responsible for the RS. In particular, this analysis provides evidence of whether modification to the electrodes or bulk of the film have a greater impact on the RS for these devices that integrate Nb metal electrodes. Several electrode and bulk conduction limited mechanisms are considered in this analysis including Poole Frenkel emission (PF), Fowler Nordheim tunneling (FN), direct tunneling (DT) and ionic conduction (IT) and these models are discussed in detail in [18] and [19]. The current density is represented as the sum of the current contributions $J_{total} = J_{PF} + J_{FN} + J_{DT} + J_{IT}$ and provides an excellent estimate to the first order of major mechanisms that contribute to the conduction current. Ohmic conduction is considered but not consistent with these measurements as the I-Vs have strong non-linearity. For practical purposes the analysis is limited to these models as they are the most expected, especially under the operating conditions examined here and the specific materials that are integrated in the heterostructure film stack. Due to the models unique voltage dependencies, extraction of the dominant mechanisms at a specific voltage is enabled and determines whether bulk or electrode limited processes are dominant and the relative impact of thermal vs. tunneling effects. Figure 8 demonstrates excellent agreement between I-V measurements and the modeled total current $I = Area * J_{total}$ subsequent to calibration of the model parameters (Table 1) for Nb-AlO$_x$-HfO$_x$-AlO$_x$-Nb (Figure 4a and 4b) and Nb-AlO$_x$-HfO$_x$-CrO$_x$-AlO$_x$-Nb (Figure 4c and 4d). The modeling methodology that is described in detail in this section uses inputs based on knowledge of the device structure and film properties to determine the dominant conduction mechanisms and uses only a few fitting parameters to describe the trap energy levels and density of trap density and electrode barrier heights. The parameters are fine-tuned until excellent agreement is obtained across the voltage range and the current components along with the total current are presented for comparison. The modeled currents are plotted here for both devices with an $Area = 250$ µm x 250 µm and the current compliance set at 1 mA and 10 mA across the 0 to 1 V range in both forward and reverse sweep directions.

The models are now described in further detail and the plausible physical explanations for the RS will be expanded on in the Sections IV-B and IV-C. In brief, a current density J_{PF} due to PF type conduction processes: conduction facilitated by the thermal enhanced emission from "trapped" charge in the bulk of the film and at the interfaces is considered. The source of PF emission can be due to various

**TABLE 1.** Conduction model: parameter values and units.

Symbol	Quantity and units	Values
ϕ_T	trap energy level (eV)	Nb-AlO$_x$-HfO$_x$-AlO$_x$-Nb: 1 mA: forward→0.18, reverse→0.17 10 mA: forward→0.22, reverse→0.17 Nb-AlO$_x$-HfO$_x$-CrO$_x$-AlO$_x$-Nb: 1 mA: forward→0.18, reverse→0.24 10 mA: forward→0.24, reverse→0.23
N_T	density of trap states (x10^{12} cm^{-2})	Nb-AlO$_x$-HfO$_x$-AlO$_x$-Nb: 1 mA: forward→1.98, reverse→2.07 10 mA: forward→0.11, reverse→2.07 Nb-AlO$_x$-HfO$_x$-CrO$_x$-AlO$_x$-Nb: 1 mA: forward→1.42, reverse→0.91 10 mA: forward→1.54, reverse→1.92
ϕ_B	barrier height (eV)	Nb-AlO$_x$-HfO$_x$-AlO$_x$-Nb: 1 mA: forward→2.61, reverse→2.61 10 mA: forward→2.65, reverse→2.61 Nb-AlO$_x$-HfO$_x$-CrO$_x$-AlO$_x$-Nb: 1 mA: forward→2.83, reverse→2.85 10 mA: forward→2.80, reverse→2.75
μ	ion mobility (cm^2/Vs)	Nb-AlO$_x$-HfO$_x$-AlO$_x$-Nb→1.1x10^{-3} Nb-AlO$_x$-HfO$_x$-CrO$_x$-AlO$_x$-Nb→8.2X10^{-4}
m_T^*	tunneling mass	Nb-AlO$_x$-HfO$_x$-AlO$_x$-Nb →0.10 Nb-AlO$_x$-HfO$_x$-CrO$_x$-AlO$_x$-Nb →0.11
ε_i	dielectric constant	Nb-AlO$_x$-HfO$_x$-AlO$_x$-Nb →10.0 Nb-AlO$_x$-HfO$_x$-CrO$_x$-AlO$_x$-Nb →8.8
T	temperature (K)	295 (room temperature), 77 (with LN$_2$ cooling)
Area	device area	250 µm x 250 µm

eV=electron Volts, cm=centimeter, K=Kelvin, V=volts, s=seconds.

charged states including ions and vacancies/defects in the ALD films or at the interfaces in the heterostructure [39]. PF type processes are typically expressed adequately with the form [18], [19]

$$J_{PF} = q\mu E N_T e^{\frac{-q\left[\phi_T - \sqrt{\frac{qE}{\pi\varepsilon_0\varepsilon_i}}\right]}{kT}} \tag{1}$$

where q is electronic charge, E is the electric field (extracted from the measurement), μ is the electronic drift mobility in the insulator (typically on the order of 10^{-4} to 10^{-3} cm^2/Vs) and set to the values in Table 1 which is kept fixed in this analysis for consistency to 1.1x10^{-3} and 8.2x10^{-4} cm^2/Vs respectively for Nb-AlO$_x$-HfO$_x$-AlO$_x$-Nb and Nb-AlO$_x$-HfO$_x$-CrO$_x$-AlO$_x$-Nb. ϕ_T is the trap energy level that spans 0.1-0.3 eV to achieve appreciable PF conduction. Its value is consistent with the location of trap and defect levels from the density functional theory (DFT) calculations for the charged states in similar films [39]. N_T is
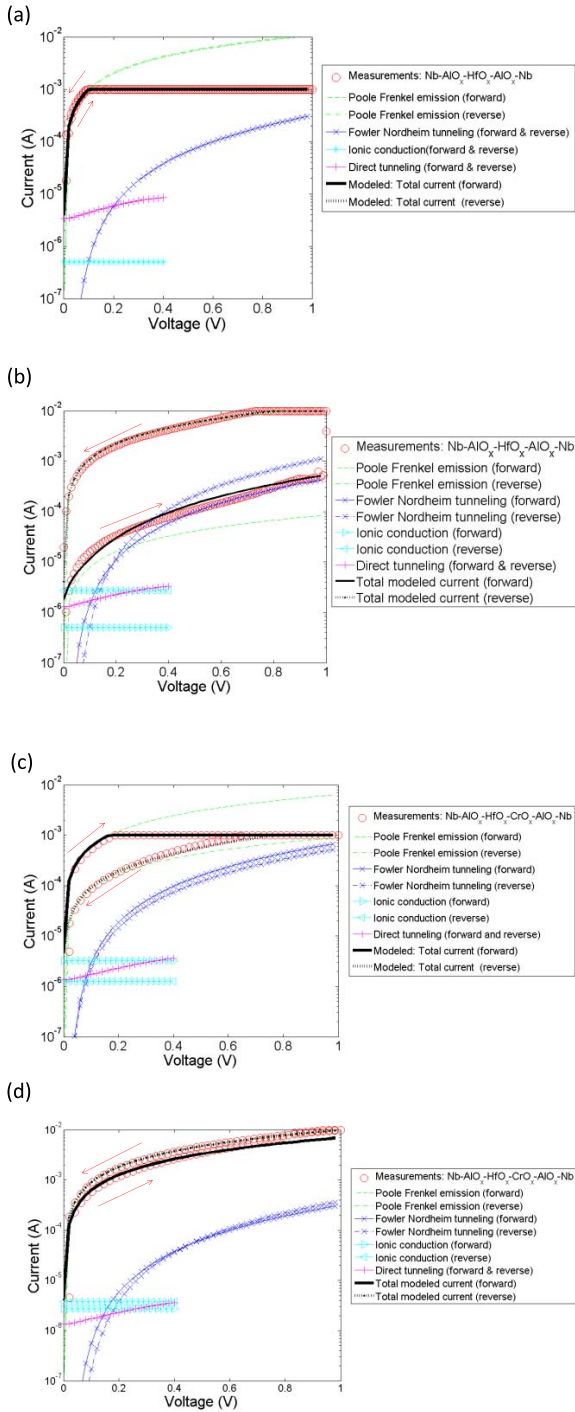
FIGURE 8. Measured (room temperature) versus modeled currents in forward and reverse spanning 0 to 1 V for 250 μm x 250 μm Nb-AlO$_x$-HfO$_x$-AlO$_x$-Nb and Nb-AlO$_x$-HfO$_x$-CrO$_x$-AlO$_x$-Nb devices. For both cases, current conduction components due to Poole Frenkel, Fowler Nordheim tunneling, direct tunneling and ionic conduction mechanisms are isolated and extracted across the voltage range. The trap energy levels, density of trap states and electrode barrier heights are extracted and estimated from the fitting. Other parameters are estimated and fixed to realistic values. Model parameters are listed in Table 1.

the average density of these trap states (ranging in density from 10^{11}-10^{13} cm^{-2} for ALD films) to provide an effective average trap spacing on the order of nanometers.

ε_o is the permittivity constant in a vacuum, and ε_i is the effective dielectric constant, and it set to 10.0 for AlO$_x$-HfO$_x$-AlO$_x$ and 8.8 for AlO$_x$-HfO$_x$-CrO$_x$-AlO$_x$. k is the Boltzmann constant and T is the operating room temperature of 295 Kelvin for this analysis. It is clear from the expression in equation (1) that calibration is required first for the exponentially dependent ϕ_T and the linearly dependent N_T, second while keeping the other parameters initially fixed as described here and subsequently fine-tuned until excellent agreement is obtained between the measured and modeled current. It is necessary to remember that equation (1) does not consider the exact location of a "trap" site within the depth of the film stack, so the extracted parameters represent the net effective average values required to achieve an excellent fitting. For practical purposes and with only 6-8 nm film thickness it can be inferred that the "traps" are distributed in the thin film stack and with a likely increased concentration at the interfaces, e.g., AlO$_x$-HfO$_x$ or CrO$_x$-HfO$_x$. Despite some of the uncertainties, the percent changes in these effective parameters (especially subsequent to RS) reveal what is happening physically as a result of the RS processes. This provides insights on, whether the RS is due to changes in the electrodes or the bulk of the film stack, the nature of these changes on the effective energy levels of the ions and vacancies/defects and if barrier lowering or increase is anticipated due to ferro-electric like effects. These issues will be described in in further detail in the next section within the context of a plausible physical model description.

The expression for current density, J_{FN} due to conduction by a FN tunneling process (tunneling that is enhanced with an applied electric field), is typically expressed adequately in [18] and [19] with the form

$$J_{FN} = \frac{q^2 E^2}{8\pi h \varnothing_B} e^{\frac{-8\pi \left(2qm_T^*\right)^{\frac{1}{2}}}{3hE}} \varnothing_B^{\frac{3}{2}} \qquad (2)$$

where m_T^* is the effective tunneling mass and set to the fixed values of 0.10 for Nb-AlO$_x$-HfO$_x$-AlO$_x$-Nb, and 0.11 with CrO$_x$ inserted. This is a good approximation for these heterostructures [40]. Planck's constant is h and the electrode barrier height is ϕ_B. From the expression in equation (2), J_{FN} is exponential and power dependent on ϕ_B, so its value is initially estimated based on knowledge of the Nb electrode work-function and the electron affinities of the materials that comprise the film stack. With m_T^* fixed, and E determined by the measurement voltage, ϕ_B is fitted to achieve a good agreement between the measured and modeled I-Vs. As FN is electric field dependent, it emerges strongly with voltage levels greater than 0.4 V where electric fields are on the MV/cm scale.

The expression for current density, J_{DT} due to DT (quantum mechanical tunneling of carriers directly across from the top Nb to bottom Nb electrodes without requiring an applied electric field), is typically expressed in [18] and [19] with

the form

$$J_{DT} = \frac{q^2}{8\pi h \varnothing_B \varepsilon} e^{\left[\frac{-8\pi\sqrt{2m_T^*(q\varnothing_B)^{\frac{3}{2}}}}{3hqE}\left(1-\left(1-\frac{V}{\varnothing_B}\right)^{\frac{3}{2}}\right)\right]}$$

(3)

where variables are as defined in the PF and FN expressions. The tunneling effective mass is m_T^*, and the value from the FN model is used. It should be noted that the difference in effective tunneling masses for DT and FN processes can vary by +/- 25% due to details of the quantum mechanical description. The DT current is calculated subsequent to a best attempt to fit the I-Vs with the PF and FN models, as DT is not expected to be primary at 6-8 nm film thickness and room temperature operation conditions.

The current density J_{IT} due to IT (current contribution due to the physical motion of charged ions) is typically expressed [18], [19] as

$$J_{IT} = J_i e^{\left[-\left(\frac{q\varnothing_B}{kT} - \frac{Edq}{2kT}\right)\right]}$$

(4)

where d is the effective ion spacing, which is readily estimated based on the extracted trap density N_T from the extracted PF conduction component. J_i is a proportional constant and adjusted based on the zero voltage current. Other variables are as already defined in the PF, FN and DT models. It is expected that in these devices that IT has a role, especially if there is any bond breakage (change in ϕ_t and N_T) and subsequent ionic transport. This warrants examination of the IT component and its interpretation not in isolation of the PF component. To complement the I-V modeling, the energy band diagrams are constructed at 0, 0.3 and 0.9 V. Values for the work-functions, energy-gaps, and valence and conduction band offsets for the Nb, AlO_x, HfO_x, and CrO_x films are estimated from sources reported in the literature based on direct measurements or theoretical modeling [29]. It should be noted that the specific values can realistically vary by +/- 10 %, depending on the specific compound and stoichiometry produced by the unique deposition processes or the presence of charged ions and vacancies/defects [39] or any interface or ferro-electric like polarization effects that may result in effective barrier lowering or increase [35].

B. RESISTIVE SWITCHING IN NB-ALO$_X$-HFO$_X$-ALO$_X$-NB HETEROSTRUCTURES

Several insights are obtained through examination of the measured and modeled I-Vs in Figures 3 and 8 and the energy band diagrams in Figures 9 and 10. First for the case of Nb-AlO$_x$-HfO$_x$-AlO$_x$-Nb, with compliance current set to 1 mA, (as described earlier), there is <1% hysteresis in the I-Vs when sweeping forward and reverse. This supports the notion that minimal changes under these measurement conditions, are occurring in the bulk of the film stack or at the electrode interfaces. All of the extracted current components are examined in order to reveal what is happening. As a reminder, under 1 mA compliance
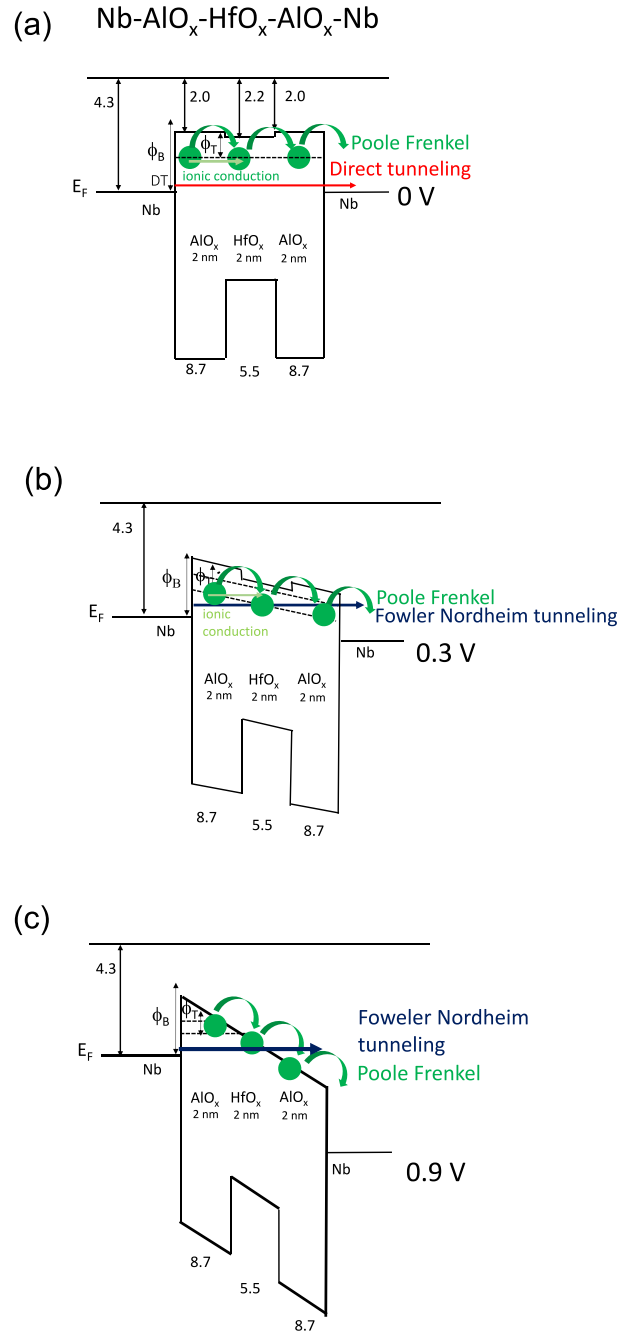
FIGURE 9. Energy band diagrams for the Nb-AlO$_X$-HfO$_X$-AlO$_X$-Nb devices consistent with the I-V measurements and modeling under (a) 0 V (b) 0.3 V and (c) 0.9 V. The diagrams describe schematically the PF, FN, DT, and IT conduction components. The effective energy barrier height ϕ_B and trap energy levels ϕ_T parameters are the estimates from the model fittings (Table 1). The energy band diagrams support a high level of PF transport with an increasing FN component with increasing voltage consistent with the I-V modeling. At neat 0 V it is clear that DT occurs but requires transport over a relatively large barrier with 6 nm film thickness. IT is apparent as a consequence of bond-breakage and transport under electric field and works in conjunction with the PF as part of the RS process.

current measurement conditions, the measured I-Vs are fit excellently considering PF as the primary conduction mechanism and using an average value of $\phi_T = 0.17$ eV and setting
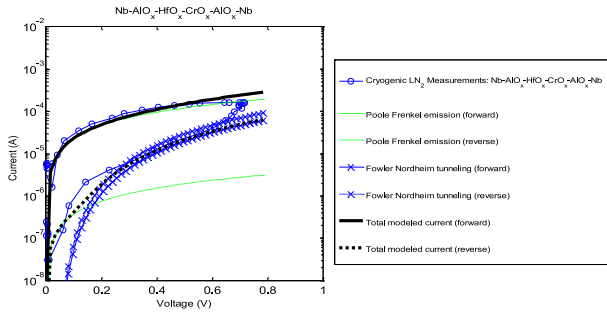
(a) Nb-AlO$_x$-HfO$_x$-CrO$_x$-AlO$_x$-Nb

(b)

(c)
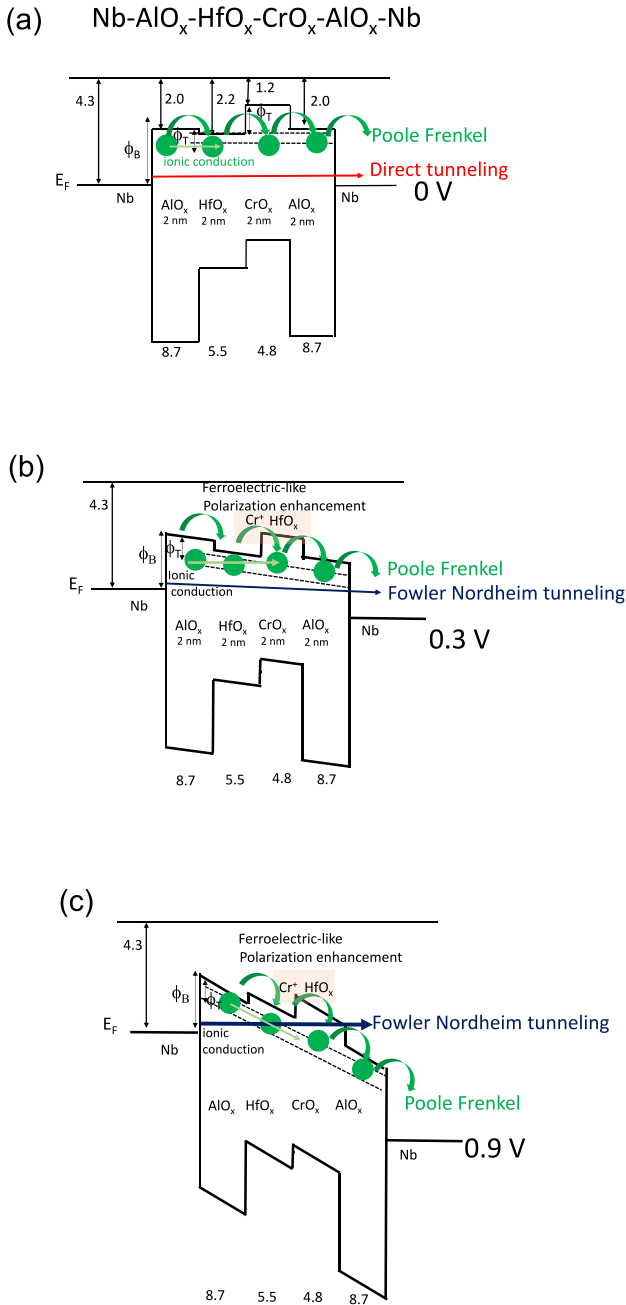
FIGURE 10. Energy band diagrams for the Nb-AlO$_x$-HfO$_x$-CrO$_x$-AlO$_x$-Nb devices consistent with the I-V measurements and modeling under (a) 0 V (b) 0.3 V and (c) 0.9 V. The effective energy barrier height ϕ_B and trap energy levels ϕ_T parameters are estimates from the model fittings (Table 1). The energy band diagram supports a high level of PF transport and an increasing FN component with elevated voltage, similar to Nb-AlO$_x$-HfO$_x$-AlO$_x$-Nb. The region of expected ferro-electric like polarization, for this case and at the CrO$_x$-HfO$_x$ interface with possible displacement of Cr$^+$ is noted. At near 0 V it is clear that DT occurs but would require tunneling transport through relatively large barrier hence reducing the quantum mechanical probability of occurrence. Similarly, IT is lower in magnitude but operates in conjunction with the PF transport as part of the RS process.

$N_T = 1.98\text{x}10^{12}\text{cm}^{-2}$, with the electrode barrier height set to $\phi_B = 2.61$ eV. The minor hysteresis is easily accounted for in the model by a commensurate increase in the value of N_t. At near zero voltage, DT is apparent and relatively strong in its contribution with μA scale current, but it is quickly overtaken by the PF component with a voltage of 50-75 mV ($\sim$2-3 kT/q). This behavior is normal and expected as with a 6.3 nm film thickness the quantum mechanical probability for DT is low. The situation is described in the band diagram in Figure 9a as well as the schematic in Figure 12a. Reducing the film thickness further, may provide increased DT, but that may not be appropriate for the design of a well-behaved memory device [14], [16], [30]. As voltage is further increased to 0.3 V, and the bands are bent further as described schematically in Figure 9b, the PF component increases exponentially, coinciding with the effective lowering in the thermal barrier required for PF. With current compliance set to 1 mA, 0.11 V is quickly reached prior to when the FN conduction component has an appreciable contribution, and based on this calculation requires a voltage exceeding 0.31 V (0.51 MV/cm). In general, the lack of appreciable hysteresis under these conditions suggests that there is insufficient electric field-strength and current flow to induce either Al-O or Hf-O bond breakage, causing minimal ion or vacancy migration or filament formation. This results in a minute physical change to the bulk of the film stack or electrodes. The PF type conduction is therefore most likely facilitated by the intrinsic ions and vacancies/defects density consistent with the extracted N_T, which is expected in ALD sub-stoichiometric films. This is especially expected in these structures that comprise two AlO$_x$-HfO$_x$ interfaces, as the density of trap sites is typically enhanced at these interfaces.

Next, with the compliance current limit increased to 10 mA and as presented in the measurements in Figure 3b, a strong RS is observed with abrupt jumps and drops in current (effectively the SET/RESET functions in a ReRAM). The currents under both forward and reverse directions are captured excellently with the models subsequent to calibration with parameters in Table 1 and as plotted in Figure 8b. The pre-RS currents are captured with a primary PF component where the initial $\phi_t = 0.17$ eV and $N_t = 2.1\text{x}10^{12}\text{cm}^{-2}$ with the electrode barrier height set to $\phi_b = 2.6$ eV, similar to the case for the measurement with current compliance set to 1 mA. To capture the large decrease in current indicative of an RS process, it requires significant primary modification of both $\phi_T = 0.22$ eV and $N_T = 1.1\text{x}10^{11}\text{cm}^{-2}$ with a slight modification to the electrode barrier height $\phi_B = 2.65$ eV. Looking closer at the I-V fittings with these conditions and where current is permitted to increase to 10 mA, it is apparent that FN emerges significantly with voltage greater than 0.4 V, 0.67 MV/cm field strength and completely exceeds the PF component at 0.7 V corresponding to an electric field strength of 1.2 MV/cm at the 6.2 nm film thickness. The situation is consistent with the band diagram in Figures 9b and 9c, which describes the situation with an increase in voltage to 0.9 V, and where a triangular potential barrier results in increasing FN tunneling with the co-existence of significant levels of PF.

FIGURE 11. Measured (cryogenic LN$_2$) versus modeled currents in forward and reverse for Nb-AlO$_x$-HfO$_x$-CrO$_x$-AlO$_x$-Nb. Extracted current conduction components consistent with PF and FN tunneling are shown. With cooling there is reduction in the total current and a consistent reduction of the *kT* dependent PF component while retaining the temperature insensitive FN tunneling current component.
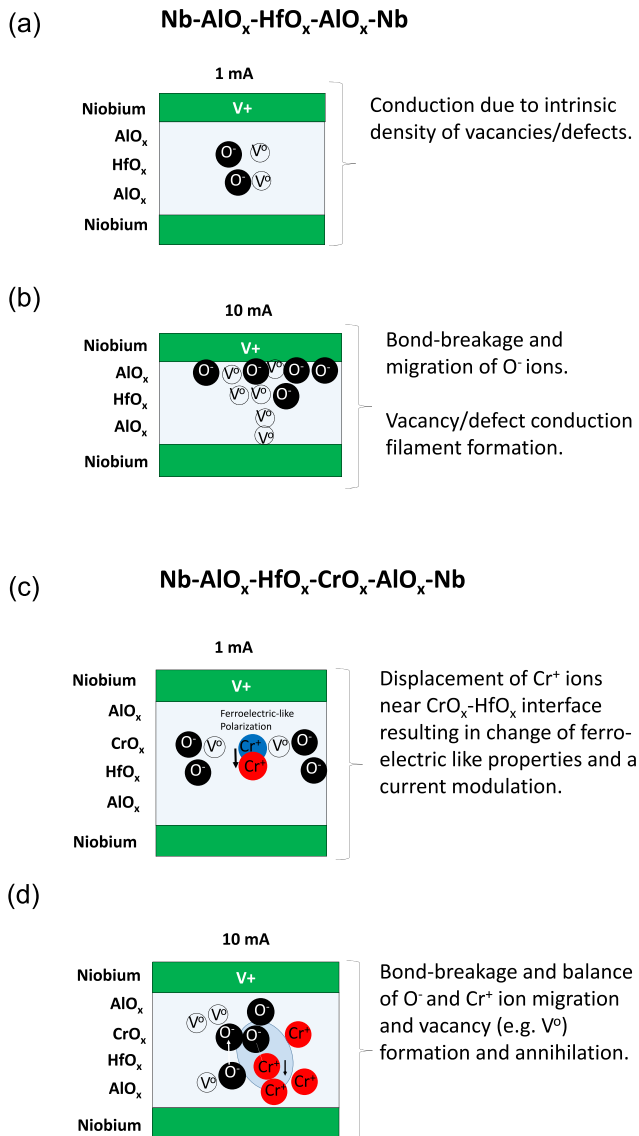
To further understand what is happening in the film stack with the RS process, a plausible scenario is examined as described schematically in Figure 12b under high current compliance and voltage conditions. The fact that the ϕ_B parameter did not require significant change to fit the I-Vs and the major changes required were to the ϕ_T and N_T, indicates changes in the AlO$_x$-HfO$_x$-AlO$_x$ film with RS and the likely contributor of the two AlO$_x$-HfO$_x$ interfaces. RS is likely due to oxygen ionic effects as described in Figure 12b, and includes under appropriate voltage and current flow conditions, the abilities to break Al-O and Hf-O bonds as well as weak bonds at the AlO$_x$-HfO$_x$ interface. This is supported by the necessary significant difference in ϕ_T and N_T between forward and reverse sweeping, while retaining a near constant ϕ_B; consistent with physical changes internal to the film stack and not of the Nb electrodes. After bond breakage and with high electric fields there can be subsequent migration of negatively charged oxygen ions towards the top Nb electrode, resulting in formation or annihilation of vacancy filaments. These vacancies in ALD films may logically comprise a mixed percentage of charged neutral V^o states as well as a smaller percentage of charged vacancy states. Recent density functional theory (DFT) calculations [39] are consistent with this notion and that these vacancies may have similar energy levels to the description observed here experimentally. With an opposite polarity voltage, (i.e., the RESET function of a memory), there is expected to be a reverse migration of the oxygen ions back towards the AlO$_x$-HfO$_x$ interfaces and subsequent recombine with the high density of vacancies and a return to the prior situation. The occurrence of these two actions would result in (1) substantial current conduction modulation consistent with what is observed here in the measurements and the need for including both PF conduction and (2) an IT component of current that does not operate in isolation. The situation is described schematically in Figure 12b and is consistent with the current understanding for RS in ALD HfO$_x$ films, albeit in this case with integration of Nb electrodes [9], [15]. Further analysis may be possible with for example atomistic molecular

dynamics simulations. While cryogenic measurements may provide further insight into the mechanisms of operation and facilitate parameter extraction and validation, cooling of the devices would likely introduce additional impacts aside from that observed at room temperature as this analysis is specific to unique operation conditions. It is relevant to note that to the best of our knowledge, this work presents the first experimental validation that a RS process in devices with Nb electrodes is possible. While it may seem obvious, there is in fact no guarantee that RS would occur as the electrodes can have a strong role on the behavior especially if they are highly prone to, for example oxidation effects [24].

C. RESISTIVE SWITCHING IN NB-ALO$_X$-HFO$_X$-CRO$_X$-ALO$_X$-NB HETEROSTRUCTURES

Next, the RS process is examined in further detail for the Nb-AlO$_x$-HfO$_x$-CrO$_x$-AlO$_x$-Nb heterostructures that integrate CrO$_x$. As described in the electrical measurements presented in Figure 3, profound differences in the RS behavior are observed. These include a gradual RS with a significant net clockwise hysteresis, supported at a significantly reduced voltage of 0.3 V and current compliance set to 1 mA. The increased non-linearity in the C-V measurements also strongly suggests that an alternate mechanism is also contributing. Similar to the case without CrO$_x$, excellent fittings between measured and modeled I-V characteristics are obtained and plotted in Figures 8c and 8d, with appropriate modification to the parameters as listed in Table 1.

These modifications provide further insight into the physical process that result in the RS. First, with current compliance set to 1 mA, the total measured current is similar, but slightly reduced with the CrO$_x$ inserted, and due to the 2 nm integrated in the film stack. To account for the hysteresis, the current conduction is captured with the identical models, with the following changes: (1) an increase of $\phi_T = 0.24$ eV, and (2) decrease of $N_T = 0.91 \times 10^{12}$ cm^{-2} and (3) setting the $\phi_B = 2.8$ eV. An increase of 0.2 eV is to account for the CrO$_x$ in the film stack that effectively increases the total barrier height. During close examination of the film stack as described in Figure 12c, in the presence of CrO$_x$, this Nb-AlO$_x$-HfO$_x$-CrO$_x$-AlO$_x$-Nb heterostructure, contains a CrO$_x$-HfO$_x$, CrO$_x$-AlO$_x$ and AlO$_x$-HfO$_x$ interface, in contrast to the two AlO$_x$-HfO$_x$ interfaces for Nb-AlO$_x$-HfO$_x$-AlO$_x$-Nb. Figure 12c describes a plausible situation for the RS observed with current compliance set to 1 mA where it is understood that under high electric field and current conditions, a soft breakdown can occur that results in, Cr-O bond breakage and Cr$^+$ migration or atomic displacement towards the HfO$_x$. It is plausible, that displacement of the Cr$^+$ at a high electric field towards the HfO$_x$ may result in a modulation of an effective ferroelectric like polarization via modification of an electrostatic doping at the interface with HfO$_x$ or an effective chemical doping. Such displacement or doping could behave similar to a ferro-electric film in altering the local electrostatic

(a)   **Nb-AlO$_x$-HfO$_x$-AlO$_x$-Nb**

1 mA

Conduction due to intrinsic density of vacancies/defects.

(b)

10 mA

Bond-breakage and migration of O$^-$ ions.

Vacancy/defect conduction filament formation.

(c)   **Nb-AlO$_x$-HfO$_x$-CrO$_x$-AlO$_x$-Nb**

1 mA

Displacement of Cr$^+$ ions near CrO$_x$-HfO$_x$ interface resulting in change of ferro-electric like properties and a current modulation.

(d)

10 mA

Bond-breakage and balance of O$^-$ and Cr$^+$ ion migration and vacancy (e.g. V^o) formation and annihilation.

FIGURE 12. Proposed physical model schematics under 1 mA and 10 mA for (a-b) Nb-AlO$_x$-HfO$_x$-AlO$_x$-Nb and (c-d) for Nb-AlO$_x$-HfO$_x$-CrO$_x$-AlO$_x$-Nb. The plausible physical mechanisms that are consistent with the measured and modeled results are described for each case and includes the balancing effects of chromium and oxygen ion migration and vacancy formation and the possibility of ferro-electric like enhancements especially at the CrO$_x$-HfO$_x$ interface. Current conduction is strong in all cases and consistent with the high density of ions and vacancies/defects that contribute to the PF transport and extracted based on the model fittings of the measured I-Vs in Figure 8 with parameters in Table I and the energy band descriptions in Figures 9 and 10.

potential of the trap energy level, resulting in subsequent modulation of the current conduction as noted on Figure 10b and 10c. Very recently, other groups have observed evidence of ferro-electric like properties along with modulation of the current conduction for doped HfO$_x$ compounds including hafnium zinc oxide, supporting this analysis [33], [34]. This notion is corroborated by evidence of partial switching in the ferroelectric polarization hysteresis loops shown earlier in Figure 6. The prevalence of large levels of PF

conduction is confirmed in the cryogenic measurements and corroborated by the fitting of the IVs comparing cryogenic to room temperature conditions in Figure 11 that have significant reduction in the thermal components with increasing dominance of the FN tunneling and retaining hysteresis in the characteristics.

Next, the configuration is examined with current compliance set to 10 mA. It is expected that both the AlO$_x$-HfO$_x$ and the CrO$_x$-HfO$_x$ interfaces contribute to the RS behavior. It is plausible, as described in Figure 12d that under these unique conditions (where the Nb-AlO$_x$-HfO$_x$-AlO$_x$-Nb had an observable RS) that there is a balance of both positively charged chromium and negatively charged oxygen ionic effects that both impact the RS process while under higher current flow and electric field conditions. In this case, however there is plausible tendency to drive recombination processes via, for example, competing oxidation and reduction that can suppress normal full filament formation. This results in a possible situation as presented in Figure 12d where normal partial filament formation towards both top and bottom electrodes is suppressed due to competition at high current density between Cr$^+$ and O$^-$ impacts to the RS. Such behavior would make a normal high/low RS process unlikely and consistent with that observed in the measurements, but current conduction would remain substantial as there is significant density of disordered ions and vacancies/defects in the film stack that would contribute to a strong PF current component. This description is therefore reasonably consistent with the measurement observations and modeling in Figures 3 and 8. The small residual counterclockwise hysteresis observed is most likely the result of a slight unequal balance of these effects. Clearly, for design of a memory device where lower voltage and current operation are preferred for technological advantage, the operating point for a memory device based on structures similar to Nb-AlO$_x$-HfO$_x$-CrO$_x$-AlO$_x$-Nb would be selected to optimize the ferro-electric like effects and enhanced RS. It is necessary to note, that while these conclusions are consistent with the measured and modeled behavior, the analysis in this manuscript does warrant further investigation by various meteorology and spectroscopy techniques, including use of atomistic molecular dynamics simulations that could further reveal the physical phenomenon that drive the current conduction and RS as well as assist in the device optimization.

V. FUTURE PROSPECTS IN VOLTAGE-CONTROLLED MEMORIES

To put these results in some perspective, Figure 13 illustrates current and future trends in voltage-controlled memory device research and development. Key figures of merit are the switching voltage and speed and suggest likely compatibility with 0.7-0.9 V CMOS [27], 0.2-0.3 V TFETs [26], or 10-20 mV SCE [8]–[9] logic. While current ReRAM solutions reported to be near production appear compatible
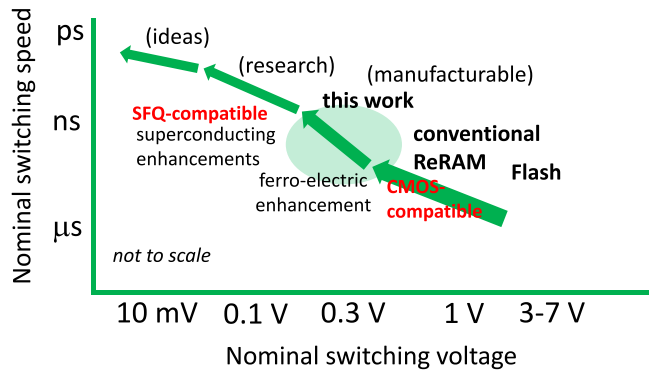
FIGURE 13. Illustrative description of current and future voltage-controlled memories considering switching voltage and speed. Shown are the advances in this work and prospects for future improvement.

with CMOS operating conditions and cross-point integration, further improvement in voltage and speed is required for compatibility with tunneling FET logic and continued improvement in energy efficiency and speed, therefore necessitating use of enhancements such as integration of ferro-electrics such as in the Nb-AlO$_x$-HfO$_x$-CrO$_x$-AlO$_x$-Nb system. It is expected that with further optimization of the heterostructure and the ferro-electric properties of the film stack, even further reduction in voltage and increase in switching speed will be obtainable. For direct compatibility with the operating conditions of SCE electronics, e.g., RSFQ circuits that switch with 20 mV and 10-20 pico-second pulses, it is necessary to investigate the impact of superconducting regime of operation that may provide for further reduction in voltage and increase in speed by harnessing Josesphson tunneling. While these concepts are largely at the basic research and idea stage, ferro-electric enhanced RS operation at room or reduced temperature appears to be near term and amenable to the manufacturing of memory cells that can be integrated in cross-point configurations.

VI. CONCLUSION

In summary, heterostructure devices integrating Nb metal and aluminum, hafnium and chromium oxide thin films are constructed by a combined sputtering and ALD process. RS is observed for the first time in devices with Nb electrodes, including specifically Nb-AlO$_x$-HfO$_x$-AlO$_x$-Nb and Nb-AlO$_x$-HfO$_x$-CrO$_x$-AlO$_x$-Nb. Insertion of CrO$_x$ in the heterostructure is observed to result in RS at lower voltage and current and increased nonlinearity in the C-V. The results support a reduced current and field threshold for RS due to inclusion of CrO$_x$ consistent with different threshold for Cr$^+$ versus O$^-$ RS processes and ferro-electric like enhancements. Insight on the conduction mechanisms and RS properties is obtained by comparing electrical measurements with conduction models and Poole-Frenkel and Fowler-Nordheim tunneling are primary transport conduction components at room temperature with the contribution of direct tunneling and ionic conduction apparent but with

reduced magnitude. The electrical measurements are consistent with high levels of ions and vacancies/defects and the formation of conduction filaments as well as the role of ferro-electric like enhancements for the case of the Nb-AlO$_x$-HfO$_x$-CrO$_x$-AlO$_x$-Nb as a consequence of the CrO$_x$ interfaces and corroborated by measured partial switching in the ferro-electric polarization loops. Measurements under liquid nitrogen conditions demonstrate retention in the RS behavior and a reduction in the thermal current components with respect to the tunneling. Low voltage and high speed operation is validated with pulsed measurements down to 20 ns pulse width/rise/fall times and the excellent retention time and endurance makes these devices a viable candidate for manufactural RS memory applications.

REFERENCES

[1] A. V. Shcherbakova *et al.*, "Fabrication and measurements of hybrid Nb/Al Josephson junctions and flux qubits with π-shifters," *Supercond. Sci. Technol.*, vol. 28, no. 2, 2015, Art. no. 025009, doi: 10.1088/0953-2048/28/2/025009.

[2] C. Granata, B. Ruggiero, M. Russo, A. Vettoliere, and P. Silvestrini, "Josephson devices for controllable flux qubit and interqubit coupling," *Appl. Phys. Lett.*, vol. 87, Nov. 2005, Art. no. 172507, doi: 10.1063/1.2115083.

[3] D. Yohannes *et al.*, "Characterization of HYPRES' 4.5 kA/cm^2 & 8 kA/cm^2 Nb/AlOx/Nb fabrication processes," *IEEE Trans. Appl. Supercond.*, vol. 15, no. 2, pp. 90–93, Jun. 2005, doi: 10.1109/TASC.2005.849701.

[4] S. K. Tolpygo *et al.*, "Advanced fabrication processes for superconducting very large-scale integrated circuits," *IEEE Trans. Appl. Supercond.*, vol. 26, no. 3, pp. 1–10, Apr. 2016, doi: 10.1109/TASC.2016.2519388.

[5] I. V. Vernik *et al.*, "Magnetic Josephson junctions with superconducting interlayer for cryogenic memory," *IEEE Trans. Appl. Supercond.*, vol. 23, no. 3, p. 1701208, Jun. 2013, doi: 10.1109/TASC.2012.2233270.

[6] B. M. Niedzierlski *et al.*, "Use of Pd–Fe and Ni–Fe–Nb as soft magnetic layers in ferromagnetic Josephson junctions for nonvolatile cryogenic memory," *IEEE Trans. Appl. Supercond.*, vol. 24, no. 4, pp. 1–7, Aug. 2014, doi: 10.1109/TASC.2014.2311442.

[7] M. A. El Qader *et al.*, "Switching at small magnetic fields in Josephson junctions fabricated with ferromagnetic barrier layers," *Appl. Phys. Lett.*, vol. 104, no. 2, 2014, Art. no. 022602, doi: 10.1063/1.4862195.

[8] D. S. Holmes, A. L. Ripple, and M. A. Manheimer, "Energy-efficient superconducting computing—Power budgets and requirements," *IEEE Trans. Appl. Supercond.*, vol. 23, no. 3, p. 1701610, Jun. 2013, doi: 10.1109/TASC.2013.2244634.

[9] M. A. Manheimer, "Cryogenic computing complexity program: Phase 1 introduction," *IEEE Trans. Appl. Supercond.*, vol. 25, no. 3, pp. 1–4, Jun. 2015, doi: 10.1109/TASC.2015.2399866.

[10] C. Newton *et al.*, "Superconductor-ionic quantum memory devices," in *Proc. Device Res. Conf.*, Newark, DE, USA, 2016, pp. 1–2, doi: 10.1109/DRC.2016.7548439.

[11] C. H. Lien *et al.*, "The highly scalable and reliable hafnium oxide ReRAM and its future challenges," in *Proc. Solid-State Integr. Circuit Technol. (ICSICT)*, Shanghai, China, 2010, pp. 1084–1087, doi: 10.1109/ICSICT.2010.5667553.

[12] J. J. Yang, D. B. Strukov, and D. R. Stewart, "Memristive devices for computing," *Nat. Nanotechnol.*, vol. 8, no. 1, pp. 13–24, 2013, doi: 10.1038/nnano.2012.240.

[13] F. Pan, S. Gao, C. Chen, C. Song, and F. Zeng, "Recent progress in resistive random access memories: Materials, switching mechanisms, and performance," *Mater. Sci. Eng. R Rep.*, vol. 83, pp. 1–59, Sep. 2014, doi: 10.1016/j.mser.2014.06.002.

[14] L. Zhu, J. Zhou, Z. Guo, and Z. Sun, "An overview of materials issues in resistive random access memory," *J. Materiomics*, vol. 1, no. 4, pp. 285–295, 2015, doi: 10.1016/j.jmat.2015.07.009.

[15] K.-C. Chang *et al.*, "Physical and chemical mechanisms in oxide-based resistance random access memory," *Nanoscale Res. Lett.*, vol. 10, no. 1, pp. 1–27, 2015, doi: 10.1186/s11671-015-0740-7.

[16] H. Akinaga and H. Shima, "Resistive random access memory (ReRAM) based on metal oxides," *Proc. IEEE*, vol. 98, no. 12, pp. 2237–2251, Dec. 2010, doi: 10.1109/JPROC.2010.2070830.

[17] D. Walczyk *et al.*, "Resistive switching behavior in TiN/HfO2/Ti/TiN devices," in *Proc. Semicond. Conf. Dresden-Grenoble (ISCDG)*, Grenoble, France, 2012, pp. 143–146, doi: 0.1109/ISCDG.2012.6360035.

[18] F.-C. Chiu, C.-Y. Lee, and T.-M. Pan, "Current conduction mechanisms in Pr2O3/oxynitride laminated gate dielectrics," *J. Appl. Phys.*, vol. 105, no. 7, 2009, Art. no. 74103, doi: 10.1063/1.3103282.

[19] F.-C. Chiu, "A review on conduction mechanisms in dielectric films," *Adv. Mater. Sci. Eng.*, vol. 2014, 2014, art. no. 578168, doi: 10.1155/2014/578168.

[20] S.-C. Chen *et al.*, "Carrier transport and multilevel switching mechanism for chromium oxide resistive random-access memory," *Electrochem. Solid State Lett.*, vol. 14, no. 2, pp. H103–H106, 2011. [Online]. Available: http://dx.doi.org/10.1149/1.3518710

[21] D. S. Jeong *et al.*, "Emerging memories: Resistive switching mechanisms and current status," *Recent Progr. Phys.*, vol. 75, no. 7, 2012, Art. no. 076502, doi: 10.1088/0034-4885/75/7/076502.

[22] J. J. Yang *et al.*, "Memristive switching mechanism for metal/oxide/metal nanodevices," *Nat. Nanotechnol.*, vol. 3, pp. 423–433, Jun. 2008, doi: 10.1038/nnano.2008.160.

[23] S.-C. Chen *et al.*, "Bipolar resistive switching of chromium oxide for resistive random access memory," *Solid-State Electron.*, vol. 62, no. 1, pp. 40–43, 2011, doi: 10.1016/j.sse.2010.12.014.

[24] L. Zhu, J. Zhou, Z. Guo, and Z. Sun, "An overview of materials issues in resistive random access memory," *J. Materiomics*, vol. 1, no. 4, pp. 285–295, 2015, doi: 10.1016/j.jmat.2015.07.009.

[25] T.-C. Chang, K.-C. Chang, T.-M. Tsai, T.-J. Chu, and S. M. Sze, "Resistance random access memory," *Mater. Today*, vol. 19, no. 5, pp. 254–264, 2016, doi: 10.1016/j.mattod.2015.11.009.

[26] O. M. Nayfeh *et al.*, "Design of tunneling field-effect transistors using strained-silicon/strained-germanium type-II staggered heterojunctions," *IEEE Electron Device Lett.*, vol. 29, no. 9, pp. 1074–1077, Sep. 2008, doi: 10.1109/LED.2008.2000970.

[27] D. A. Antoniadis *et al.*, "Continuous MOSFET performance increase with device scaling: The role of strain and channel material innovations," *IBM J. Res. Develop.*, vol. 50, nos. 4–5, pp. 363–376, Jul. 2006, doi: 10.1147/rd.504.0363.

[28] Y. Hou *et al.*, "Doping profile modification approach of the optimization of HfOx based resistive switching device by inserting AlOx layer," *Sci. China Inf. Sci*, vol. 58, no. 6, pp. 1–7, 2015, doi: 10.1007/s11432-015-5283-0.

[29] J. Robertson, "High dielectric constant gate oxides for metal oxide Si transistors," *Rep. Progr. Phys.*, vol. 69, no. 2, pp. 327–396, 2005, doi: 10.1088/0034-4885/69/2/R02.

[30] O. M. Nayfeh, "Nonvolatile memory devices with colloidal, 1.0 nm silicon nanoparticles: Principles of operation, fabrication, measurements, and analysis" Ph.D. dissertation, Dept. Elect. Eng. Comput. Sci., Massachusetts Inst. Technol., Cambridge, MA, USA, 2009.

[31] Y. Takeshi, T. Kuribayashi, M. Gomi, T. Shundo, and Y. Sakakibara, "Preparation and investigation on magneto-electric effect of Cr2O3 thin films," *Adv. Mater. Res.*, vols. 11–12, pp. 133–136, Jan. 2006. [Online]. Available: http://dx.doi.org/10.4028/www.scientific.net/AMR.11-12.133

[32] P. Borisov, T. Ashida, T. Nozaki, M. Sahashi, and D. Lederman, "Magnetoelectric properties of 500-nm Cr2O3 films," *Phys. Rev. B, Condens. Matter*, vol. 93, no. 17, 2016, Art. no. 174415, doi: 10.1103/PhysRevB.93.174415.

[33] M. H. Park *et al.*, "Ferroelectricity and antiferroelectricity of doped thin HfO2-based films," *Adv. Mater.*, vol. 27, no. 11, pp. 1811–1831, 2015, doi: 10.1002/adma.201404531.

[34] Z. Fan *et al.*, "Ferroelectricity and ferroelectric resistive switching in sputtered Hf0.5Zr0.5O2 thin films," *Appl. Phys. Lett.*, vol. 108, no. 23, 2016, Art. no. 232905, doi: 10.1063/1.4953461.

[35] J. J. Cuomo, R. J. Gambino, and R. Rosenberg, "The influence of bias on the depostion of metallic films in RF and DC sputtering," *J. Vacuum Sci. Technol.*, vol. 11, no. 1, pp. 34–40, 1974, doi: 10.1116/1.1318617.

[36] H. Kim, H.-B.-R. Lee, and W.-J. Maeng, "Applications of atomic layer deposition to nanofabrication and emerging nanodevices," *Thin Solid Films*, vol. 517, no. 8, pp. 2563–2580, 2009, doi: 10.1016/j.tsf.2008.09.007.

[37] J. Tao *et al.*, "Extrinsic and intrinsic frequency dispersion of high-k materials in capacitance-voltage measurements," *Materials*, vol. 5, no. 6, pp. 1005–1032, 2012, doi: 10.3390/ma5061005.

[38] C.-H. Lu *et al.*, "Characteristics and mechanism of tunable work function gate electrodes using a bilayer metal structure on SiO/sub 2/ and HfO/sub 2/," *IEEE Electron Device Lett.*, vol. 26, no. 7, pp. 445–447, 2005, doi: 10.1109/LED.2005.851232.

[39] P. J. Hasnip *et al.*, "Density functional theory in the solid state," *Philosophical Trans. Roy. Soc. A Math. Phys. Eng. Sci.*, vol. 372, no. 2011, 2014, Art. no. 20130270, doi: 10.1098/rsta.2013.0270.

[40] W. J. Zhu, T.-P. Ma, T. Tamagawa, J. Kim, and Y. Di, "Current transport in metal/hafnium oxide/silicon structure," *IEEE Electron Device Lett.*, vol. 23, no. 2, pp. 97–99, Feb. 2002, doi: 10.1109/55.981318.

LANCE LERUM was born in CA, USA, in 1995. He received the B.S. degree in electrical engineering from the University of California at San Diego, CA, USA, in 2017, where he is currently pursuing the M.S. degree in electrical engineering. In 2016, he joined the Space and Naval Warfare Systems Command Center, CA, USA, where his research was supported by the Naval Research Enterprise Internship Program. His current research interests include resistive memory devices, antenna design, and RF communication circuit and system design

MOHAMMED FAHEM was born in Baghdad, Iraq, in 1989. He is currently pursuing the B.S. degree in electrical engineering with San Diego State University (SDSU). He had an overt desire to join the SPAWAR team; the Space and Naval Warfare System Command Center, CA, USA, where he was supported by the SDSU Research Foundation Program. His current research interests include antenna design, analog and pulse communication systems, and RF communication circuit and system design.

OSAMA M. NAYFEH (M'02) received the B.Sc. degree from the University of Illinois at Urbana–Champaign and the M.Sc. and Ph.D. degrees from the Massachusetts Institute of Technology. He is the Quantum Memory Integrated Product Team Leader with the Space and Naval Warfare Systems Center Pacific.

C. DAVE REES is the In House Laboratory Science and Technology Program Manager with the Space and Naval Warfare Systems Center Pacific.

AYAX D. RAMIREZ is the Advanced Systems and Applied Sciences Division Head with the Space and Naval Warfare Systems Center Pacific. He is also a part-time Professor of Physics with Southwestern College, Chula Vista, CA, USA.

KENNETH S. SIMONSEN is the Systems of Systems and Platform Integration Division Head with the Space and Naval Warfare Systems Center Pacific.